



Ni-Co-P nanosheets in-situ grown at macroporous nickel mesh with promising performance for hydrogen evolution reaction in alkaline medium

An Huang¹ · Peijun Liu¹ · Peihua Lin¹ · Ming Fang¹ · Guanping Jin¹ · Chunnian Chen¹

Received: 8 October 2022 / Revised: 7 February 2023 / Accepted: 8 February 2023 / Published online: 4 March 2023
© The Author(s), under exclusive licence to Springer-Verlag GmbH Germany, part of Springer Nature 2023

Abstract

Pursuing efficient, economical, and stable electrodes on hydrogen production by water splitting is of great significance for new energy sources. In this work, Ni-Co-P self-supported electrocatalyst at macroporous nickel mesh electrode (NCP/NM) was prepared by a combination of hydrothermal and phosphorylation reactions. The Ni-Co with spherical form was in-situ deposited on nickel mesh (NM) in the alkaline environment provided by aqueous ammonia. The phosphorylation process offered the doping of P elements at the surface of Ni-Co, forming irregular nanosheets. The fabricated electrode only needed to be supplied with an overpotential of 126 mV to respond to a current density of 10 mA cm⁻² in 1 M KOH electrolyte. The lower Tafel slope (87.62 mV dec⁻¹) and charge transfer resistance suggested NCP/NM electrode exhibited competitive hydrogen evolution reaction (HER) kinetics. In addition, NCP/NM showed good durability and applicability in the alkaline medium. The increase in electrochemical active area, the fast electron transfer without binder, and the synergistic effect among Ni, Co, and P collectively contributed to the electrode with competitive hydrogen production performance. The inspiring HER performance of NCP/NM, as well as the low-cost and easily accessible synthesis method, displayed the enormous potential and advantages of its application in industrial water splitting for hydrogen production.

Keywords Ni-Co-P nanosheets · Electrocatalysis · In-situ growth · HER

Introduction

Nowadays, the increasing use of fossil fuels has not only brought a shortage of fossil fuels as a non-renewable resource but also exposed people to several serious problems, such as greenhouse gas emissions and environmental degradation [1, 2]. Therefore, alternative and clean energy sources are being urgently sought. As a clean energy source with high energy density and non-polluting combustion, hydrogen energy has attracted increasing attention and studies [3–5]. Compared with other mainstream steam methane reforming and coal gasification for hydrogen production

[6, 7], electrocatalytic water splitting is more favored as it requires only eco-friendly electricity and sufficient water supply. In addition, the oxygen evolution reaction (OER) and hydrogen evolution reaction (HER) occur separately at the anode and cathode, ensuring the cleanliness of the whole process and the products [8, 9]. However, due to the superpotential of HER at the cathode consumes more electrical energy, many scholars focus on the preparation of various functional cathodes to decrease the superpotential. As a well-known fact, platinum group metals and their alloys or metal oxides are excellent catalysts for HER, but their widespread applications for industries are limited by low element abundance and high extraction costs [10, 11]. Therefore, it is highly urgent to develop high-activity and continuously durable non-precious metal electrocatalysts for HER.

Up to now, various studies for HER have been conducted on this aim [12]. For instance, transition metal and their alloys [13, 14], transition metal phosphides [15], carbides [16], nitrides [17], and sulfides [18] have been studied as effective electrocatalysts by different modification means. Especially, benefiting from the wide distribution and high

✉ Guanping Jin
jgp@hfut.edu.cn

✉ Chunnian Chen
chencn@hfut.edu.cn

¹ Anhui Key Lab of Controllable Chemical Reaction & Material Chemical Engineering, School of Chemistry and Chemical Engineering, Hefei University of Technology, Hefei 230009, China

abundance of nickel (Ni) and cobalt (Co) elements on the geological surface, Ni-based and Co-based electrocatalysts show excellent catalytic performance and stability in alkaline solutions, which have been extensively investigated in recent years and have been expected to replace precious metals to achieve efficient HER [19–21]. And the electronic structure and d-spectrum generation centers of transition metal-based catalysts can be modulated by non-metallic intercalation, which provides a realizable and effective tactic to enhance the activity of electrocatalysts [22]. In addition, metal oxides with spinel structures are considered as promising electrocatalysts for water splitting because of their good physicochemical properties and electrocatalytic activity [23]. On the other hand, excellent electrocatalysts would be combined with high-conductive substrates for sustained water splitting. With the merits of high conductivity, superb specific surface area, and favorable HER behavior, three-dimensional porous nickel foam (NF) is widely chosen as the conductive substrate. For instance, Wang et al. [24] successfully manufactured self-supported electrocatalysts of NF with P-modified Co_3O_4 nanowire arrays which were adjusted with different P doping ratios. And the work revealed that P-doping can change the electronic structure of catalysts, showing excellent performance in overall water splitting. Cheng et al. [25] fabricated P-Ni Co_2O_4 /NF electrocatalyst via a facile hydrothermal and a subsequent phosphatizing treatment, which demonstrated that P incorporation helped to improve HER kinetics and enhance HER activity.

Considering the production of hydrogen in industrial water splitting, the migration of cations from the solution during HER will move to the cathode. Part of them reacts with the rich hydroxyl groups on the cathode surface to generate precipitates that wrap the active sites on the porous substrate, making the electrocatalyst prone to toxicity and ineffectiveness. The three-dimensional porous NF matrix undoubtedly accelerates the above reaction, which is contrary to our original intention. In addition, ordinary NF exists drawbacks such as easy deformation under pressure and brittle after annealing, so it is only suitable for limited mild modification means [26]. Therefore, a self-supporting matrix electrocatalyst conforming to the characteristics of large pore size and rigidity is urgently needed for the HER process in actual water splitting to achieve a win–win situation of hydrogen energy supply and electrode consumption reduction in an alkaline medium. Thus, we chose NM as a substrate to face HER performed in complex electrolytes.

Inspired by the above ideas and combined with the practical needs of water splitting, we designed a Ni-Co-P nanosheet electrocatalyst grown at macroporous NM for HER in an alkaline medium by hydrothermal method and phosphorylation. With promising HER electrocatalytic performance in 1 M KOH electrolyte, NCP/NM was able to achieve 10 mA cm^{-2} with only 126 mV overpotential.

Continuous constant voltage electrolysis and multi-step constant current electrolysis confirmed the promising durability and applicability of the electrode. The related physicochemical analysis and characterization showed little change in the micromorphological structure and physical phase after long-term working, corroborating the favorable structural stability of the electrolysis. NCP/NM prepared by the above strategy provided an inexpensive, high electrocatalytic performance, and durable alternative cathode for hydrogen production in an alkaline medium.

Experimental

Materials

Nickel chloride hexahydrate ($\text{NiCl}_2 \cdot 6\text{H}_2\text{O}$), cobalt chloride hexahydrate ($\text{CoCl}_2 \cdot 6\text{H}_2\text{O}$), sodium hypophosphite monohydrate ($\text{NaH}_2\text{PO}_2 \cdot \text{H}_2\text{O}$), and commercial Pt/C (10 wt%) were bought from Aladdin Reagent (Shanghai, China). Ammonium hydroxide ($\text{NH}_3 \cdot \text{H}_2\text{O}$, 25–28 wt%), hydrochloric acid (HCl), and potassium hydroxide (KOH) were supplied via Sinopharm Chemical Reagent Co., Ltd. All chemical reagents were of the analytical variety and were employed without purifying. Bare nickel mesh with diamond-shaped holes (b-NM) and commercial nickel mesh with diamond-shaped holes (c-NM) were purchased from Hongze (Jiangsu) Technology Co., Ltd.

Synthesis of NC/NM, NCO/NM, and NCP/NM

To remove surface oxides and contaminants, b-NM ($1 \text{ cm} \times 2 \text{ cm} \times 0.1 \text{ cm}$) was ultrasonically bathed in 4 wt% HCl solution and acetone, each for 20 min. All samples were washed with deionized water before that being immediately transferred for the next procedure. The 22 mL of deionized water was mixed with 0.1 mol each of $\text{NiCl}_2 \cdot 6\text{H}_2\text{O}$ and $\text{CoCl}_2 \cdot 6\text{H}_2\text{O}$ to dissolve them and stirred the mixture for a while. A total of 8 mL $\text{NH}_3 \cdot \text{H}_2\text{O}$ as a complexing medium was added before the mixture was sonicated, forming a homogeneous solution. Subsequently, a 50 mL Teflon-lined stainless steel autoclave was loaded with the above solution and b-NM. After being maintained at $120 \text{ }^\circ\text{C}$ for 12 h, the hydrothermal reaction was left to spontaneously drop to ambient temperature. Later, a vacuum oven was used to dry the synthetic catalytic electrode overnight at $60 \text{ }^\circ\text{C}$ after it had been cleaned several times with deionized water. The above electrode loaded with an electrocatalyst was labeled as NC/NM. In the next step, NC/NM and 200 mg $\text{NaH}_2\text{PO}_2 \cdot \text{H}_2\text{O}$ were kept with quartz vessels in the downstream and upstream of a tube furnace, separately. The target electrodes were obtained by heating to $350 \text{ }^\circ\text{C}$ under a nitrogen atmosphere and holding for 3 h and then

letting the temperature drop naturally to ambient temperature. The produced catalytic electrodes were cleaned with deionized water and ethanol several times before being vacuum-dried at 60 °C for the duration of the night and labeled as NCP/NM. To compare the effect of phosphorylation or not on the catalytic electrodes, contrasted electrodes were fabricated under the same requirements without the addition of $\text{NaH}_2\text{PO}_2 \cdot \text{H}_2\text{O}$. The products obtained under the above conditions were labeled as NCO/NM. The loading mass of Ni-Co-P nanosheets on NM was calculated as about 5.0 mg cm^{-2} from the weight change. The loadings for NC/NM and NCO/NM were about 4.7 mg cm^{-2} and 5.0 mg cm^{-2} , respectively.

For further comparison, commercial Pt/C was loaded on an NM electrode. In detail, 10 mg Pt/C was dispersed in a solution mixed with 250 μL isopropanol, 700 μL deionized water, and 50 μL 5% Nafion. The above mixture was sonicated for 60 min to form a homogeneous ink. Afterwards, all ink was evenly applied to NM and allowed to dry naturally to obtain Pt/C/NM.

Characterizations

An X'Pert Pro MPD diffractometer was utilized to obtain X-ray diffraction (XRD) data by using a Cu target ($\lambda = 0.154 \text{ nm}$) with a scan range from 5 to 80°. Al K α radiation was applied to conduct X-ray photoelectron spectroscopy (XPS) on a Thermo ESCALAB250Xi instrument. The scanning electron microscopy (SEM, Gemini 500) and the equipped energy dispersive spectroscopy (EDS, Aztec UltimMax 100) were used to investigate the structure and morphology of the produced catalytic electrodes. Transmission electron microscope (TEM) and high-resolution TEM (HRTEM) measurements were further analyzed for the morphology and phase structure of the electrocatalysts which were ultrasonically stripped.

Electrochemical measurements

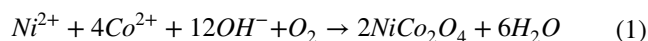
To minimize the effect of capillary phenomena, all samples were encapsulated with epoxy resin before electrochemical testing to achieve a $1 \text{ cm} \times 1 \text{ cm}$ conductive section in solution. The CHI760E electrochemical workstation served as a controller for electrochemical tests in a typical three-electrode system to collect relevant electrochemical data. The measured samples, graphite rod, and Hg/HgO electrode were employed as the working electrode, counter electrode, and reference electrode in the system, respectively. Simultaneously, 1 M KOH solution saturated with nitrogen was used as the electrolyte. For direct comparison of standardized potentials, the Nernst equation was used to translate each test potential reported in this investigation to the reversible hydrogen electrode (RHE) [27]:

$E(\text{RHE}) = E(\text{Hg}/\text{HgO}) + 0.098 + 0.059\text{pH}$. With a scan speed of 5 mV/s, all samples were tested for their HER performance using linear sweep voltammetry (LSV), and data were collected by 100% manual iR correction. Tafel plots were obtained by fitting the data of LSV to the Tafel equation. By using cyclic voltammetry (CV) measurements in the non-Faraday current zone with scan rates of 20–80 mV/s, the electrochemical double-layer capacitances (C_{dl}) of the catalytic electrodes were evaluated. With an amplitude of 5 mV and an overpotential of 200 mV, electrochemical impedance spectroscopy (EIS) was conducted in the frequency range of 100 kHz to 0.1 Hz. Continuous electrolysis was implemented by chronoamperometry for 10 h to assess the durability of the optimal electrocatalyst. In addition, multi-step chronopotentiometry was used to evaluate electrocatalytic applicability and stability at different current densities.

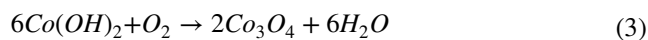
Results and discussion

Synthesis principle

Figure 1 provides a clear illustration of the proposed method for synthesizing catalytic electrodes. During the initial phase of the hydrothermal reaction, unlike the typical synthesis routes of NiCo_2O_4 loading on a substrate [28–30], ammonia solution was used to replace urea and ammonium fluoride as a solvent for the hydrothermal reaction to obtain the electrocatalyst precursor, because it provided ammonium and hydroxyl groups that complex and generate metal hydroxides with metals. In the above step, the main reaction equation at the electrode could be illustrated below:



The precursor was subsequently phosphorylated by chemical vapor deposition (CVD), while the metal hydroxide on the precursor was subjected to heat to produce metal oxides. After natural cooling, the hue of the electrode surface changed from rosy color to black (Fig. S1). The possible reaction on the electrode at this step was the following equation:



Physicochemical properties

To detect and analyze the phase composition and crystal structure of various catalytic electrodes, XRD technology was performed. In Fig. S2, the (111), (200), and (220) planes of Ni (ICDD:00–004–0850) can be matched exactly to the

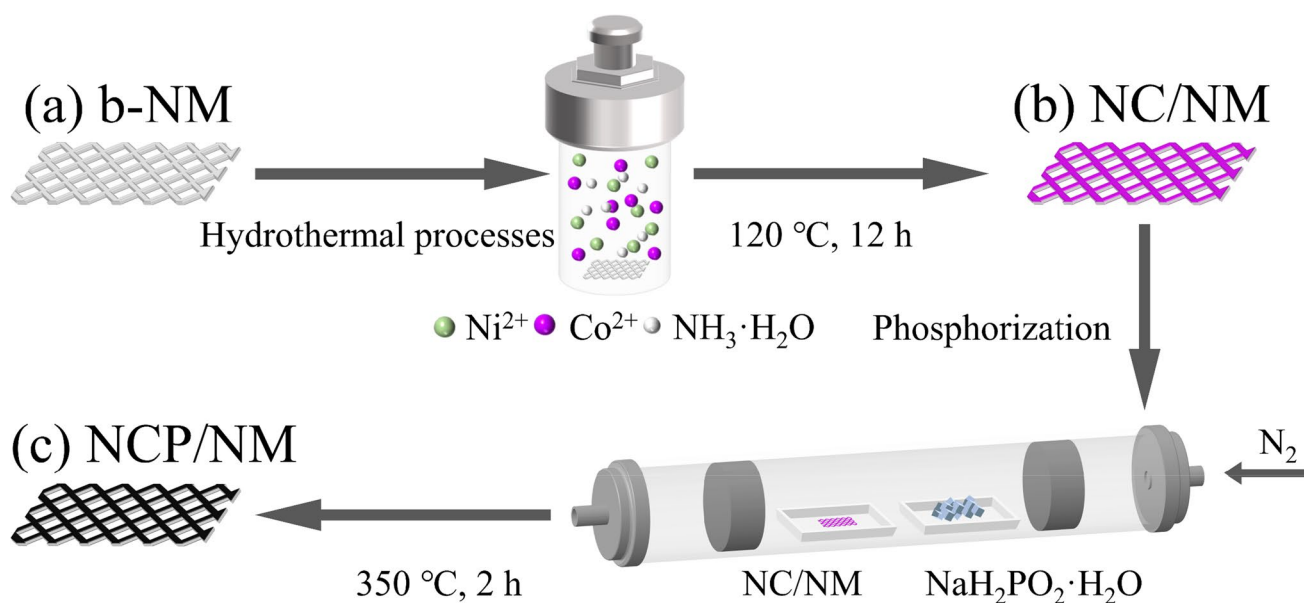


Fig. 1 Schematic illustration of the synthesis steps of catalytic electrodes

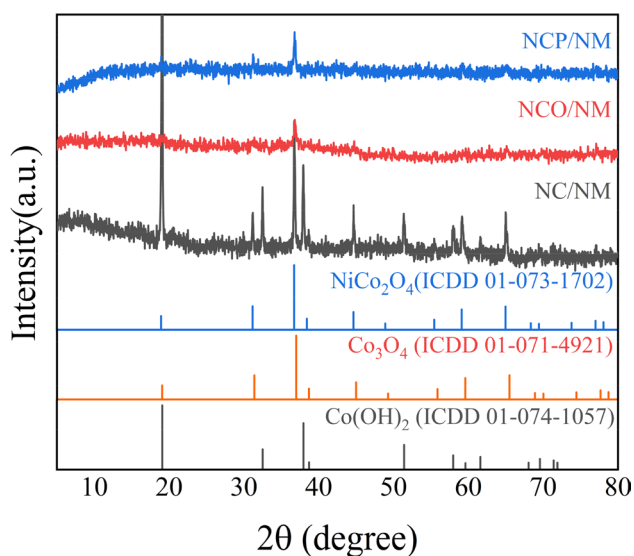


Fig. 2 XRD patterns of NC/NM, NCO/NM, and NCP/NM

peaks of b-NM appearing at $2\theta = 44.5^\circ$, 51.8° , and 76.4° , respectively. After the hydrothermal reaction process, the (001), (100), and (011) planes of Co(OH)_2 (ICDD: 01-074-1057) can be precisely correlated to the strong diffraction peaks which appeared at 19.05° , 32.47° , and 37.95° , as illustrated in Fig. 2 (black). Simultaneously, $2\theta = 31.2^\circ$, 36.7° , and 65.0° of the other main peaks are corresponded to (220), (311), and (440) planes of NiCo_2O_4 phase (ICDD: 01-073-1702). This indicates that a mixture of Co(OH)_2 and NiCo_2O_4 can be obtained by hydrothermal reaction. The curve of phosphorylated NCP/NM displays three diffraction

peaks at 18.9° , 31.2° , and 36.7° , which can be ascribed to the (111), (220), and (311) planes of NiCo_2O_4 or Co_3O_4 (ICDD: 01-071-4921), since the diffraction peaks of NiCo_2O_4 and Co_3O_4 at diffraction angle above are quite close [31]. The XRD pattern of NCO/NM is also the same as above. It can be observed that the intensity of the dominant diffraction peaks of NCP/NM and NCO/NM are diminished when compared with that of NC/NM, demonstrating a low degree of crystallization in the material after a period of calcination.

As shown in Fig. 3a–d, the SEM technique was employed to detect the surface morphology characteristics of electrocatalysts. The SEM image of b-NM (Fig. 3a) shows concave and uneven structures, and there are no obvious external objects on the surface. Apparently, a number of rough microspheres (particle size of ~ 300 – 400 nm) are grown on b-NM after hydrothermal reaction, as shown in Fig. 3b. The microstructure of NCO/NM catalytic electrode is exhibited in Fig. 3c. When compared to the sample without calcination treatment, it is obvious that the micromorphological structure of the small spheres dispersed on the substrate is no significant change except for a reduction in particle size (particle size of ~ 200 – 300 nm). Interestingly, after phosphorylation by the CVD process, the surface structures of NC/NM collapse significantly and the microspheres on the substrate become nanosheet-like structures (Fig. 3d). This increases the number of active sites for hydrogen precipitation, undoubtedly. Meanwhile, to characterize the elemental composition of the NCP/NM electrode surface, an EDS analysis was conducted. Figure 3e presents Ni, Co, P, and O elemental mapping images, demonstrating their homogeneous distribution across the substrate surface. In addition, the

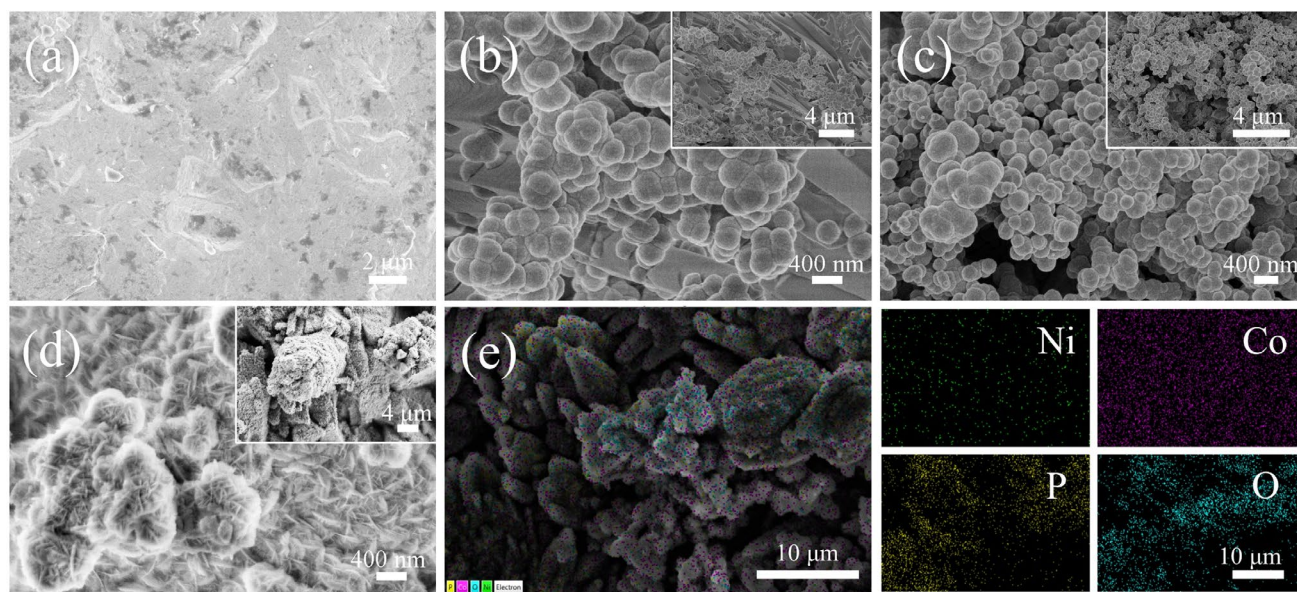


Fig. 3 SEM images of the **a** a-NM, **b** NC/NM, **c** NCO/NM, and **d** NCP/NM; **e** EDS mappings of NCP/NM catalytic electrode

effective synthesis of NCP/NM is validated by the elemental composition of Ni, Co, P, and O, which can be seen in Fig. S3. TEM analyses were conducted to further observe the microstructure and chemical composition of NCP/NM. Figure 4a distinctly displays several irregular nanosheets, which is consistent with the SEM image. In Fig. 4b, the lattice fringes of $d=0.24$ nm were clearly depicted by the HRTEM technique, which is in accordance with the distances of the (311) planes of NiCo_2O_4 or Co_3O_4 , implying metal oxides occupy the major components of electrocatalysts. Figure 4c confirms that Ni, Co, P, and O are evenly dispersed in nanosheets, which is in line with the result of SEM (Fig. 3e), further revealing their uniform distribution in the whole electrocatalyst.

XPS technique, as an effective method to investigate the chemical properties of material surfaces, was adopted to further analyze the chemical composition and elemental valence of fabricated electrodes surface. As depicted in Fig. 5a, XPS survey spectra of three electrodes reveal the presence of elements Ni, Co, C, and O on the electrode's surface. Here, carbon indicates calibration and oxygen derives from the synthesized reagent, and the partial oxidation of the sample surface may also contribute to the presence of oxygen. Notably, the curve of NCP/NM additionally shows the presence of element P. Figure 5b–d is the high-resolution XPS spectra for electrodes. The Ni 2p spectrum of NCP/NM represents the binding energy peaks at 856.5 eV and 873.75 eV associated with Ni 2p_{3/2} and Ni 2p_{1/2}, respectively [32]. Meanwhile, there is a 17.25 eV difference in their binding energies, which further proves

the existence of Ni^{2+} . Also, two extra binding energy peaks can be ascribed to the shake-up satellite peaks of Ni 2p_{3/2} and Ni 2p_{1/2}, respectively, with positioned at 862.1 eV and 881.05 eV. As for the Co 2p spectrum of NCP/NM, the appearance of two main peaks at 781.45 eV and 797.7 eV can be assigned to Co 2p_{3/2} and Co 2p_{1/2}, correspondingly [33]. Specifically, the appearance of peaks at the binding energy of 781.05 eV and 796.95 eV can be attributed to Co^{3+} cation. Similarly, it is reasonable to attribute the peaks appearing at 782.95 eV and 798.4 eV to the Co^{2+} cation. This demonstrates the coexistence of Co^{3+} and Co^{2+} on the electrode surface [34, 35]. The residual peaks at 786.7 eV and 803.4 eV can be explained by the satellite peaks arising from high spin Co shake-up excitation. In Fig. 5d, two dominant peaks at 129.75 eV and 133.65 eV are portrayed at the XPS spectrum of P 2p for NCP/NM, compared with NC/NM and NCO/NM, which correspond to metal phosphides (P-M) on the electrode surface and P-O bond of phosphates [36, 37], respectively. It reflects the successful doping of P onto the catalytic electrode surface after phosphorylation as well as its presence in two forms. Moreover, note that the peaks of Ni 2p_{3/2} and Co 2p_{3/2} for NCP/NM show shifts of higher binding energies for 0.62 eV and 0.67 eV compared with untreated NC/NM; however, the peaks of NCO/NM show no significant shift. The result indicates a decrease in the electron density and an increase in electronegativity of Ni and Co species after phosphorylation, which is expected to enhance the electrocatalytic activity [38].

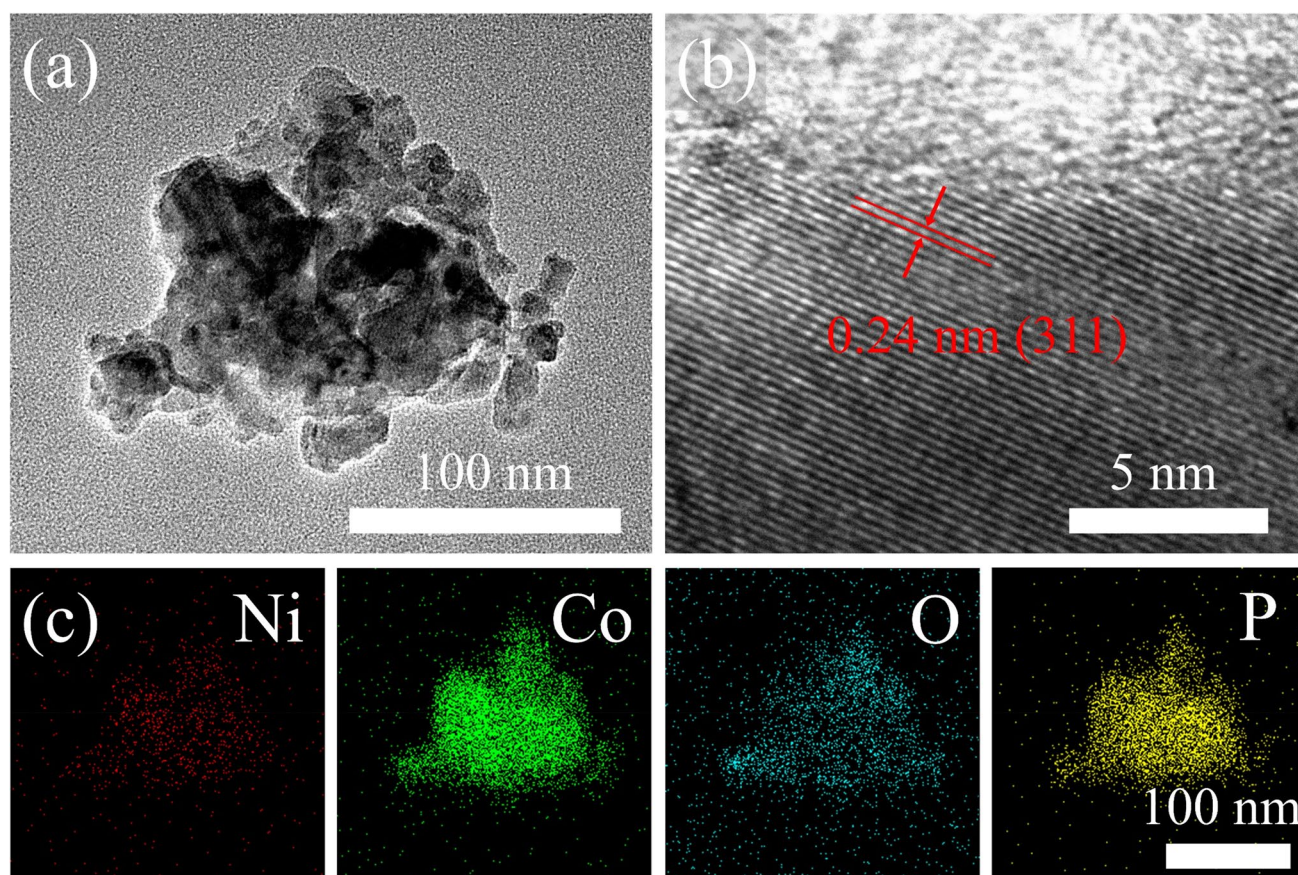


Fig. 4 **a** TEM image, **b** HRTEM image, and **c** elemental mapping of NCP/NM

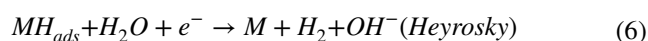
HER performance

The electrocatalytic activities of the relevant electrodes were respectively evaluated in 1 M KOH. Figure 6a shows the LSV curves with 100% manual iR compensation of all samples. The sharp increasing current density for HER can be clearly seen at NCP/NM with the increasing driving voltage, indicating a favorable kinetic and thermodynamic activity [39]. To quantify their catalytic activities, the driving overpotentials required at current densities of 10 and 100 mA cm⁻² are listed in Fig. 6b. The required overpotentials are 73 mV (Pt/C/NM), 126 mV (NCP/NM), 147 mV (c-NM), 269 mV (NCO/NM), 309 mV (NC/NM), and 345 mV (b-NM) at 10 mA cm⁻², respectively. Similarly, the overpotentials of the above electrodes are 230, 208, 281, 353, 421, and 471 mV for 100 mA cm⁻². From above the facts, except for Pt/C/NM, NCP/NM shows the lowest overpotentials for HER in an alkaline medium, which is competitive with some non-precious metal-supported electrodes reported in recent years (Table S1). It should be pointed out that the catalytic activity of NCP/NM at higher current densities even surpasses that of Pt/C/NM.

It is widely acknowledged that the Tafel slope is an essential parameter to understand the HER kinetic process. The Tafel slope is fitted by the LSV data with 100% manual iR compensation via the following Tafel equation [40]:

$$\eta = a + b \log |j| \quad (4)$$

where, respectively, η , b , and j stand for overpotential, Tafel slope, and current density. The presented results are well-fitted linear segment in Fig. 6c. As expected, except for Pt/C/NM, NCP/NM exhibits the lowest Tafel slope (87.62 mV dec⁻¹) compared with that of c-NM (88.17 mV dec⁻¹), NCO/NM (93.08 mV dec⁻¹), NC/NM (93.65 mV dec⁻¹), and b-NM (94.22 mV dec⁻¹), demonstrating the fastest charge transfer processes and kinetic processes in 1 M KOH. Generally, in an alkaline medium, the HER mechanism may involve two processes (Volmer-Heyrosky and Volmer-Tafel mechanism) by the following three basic steps [41]:



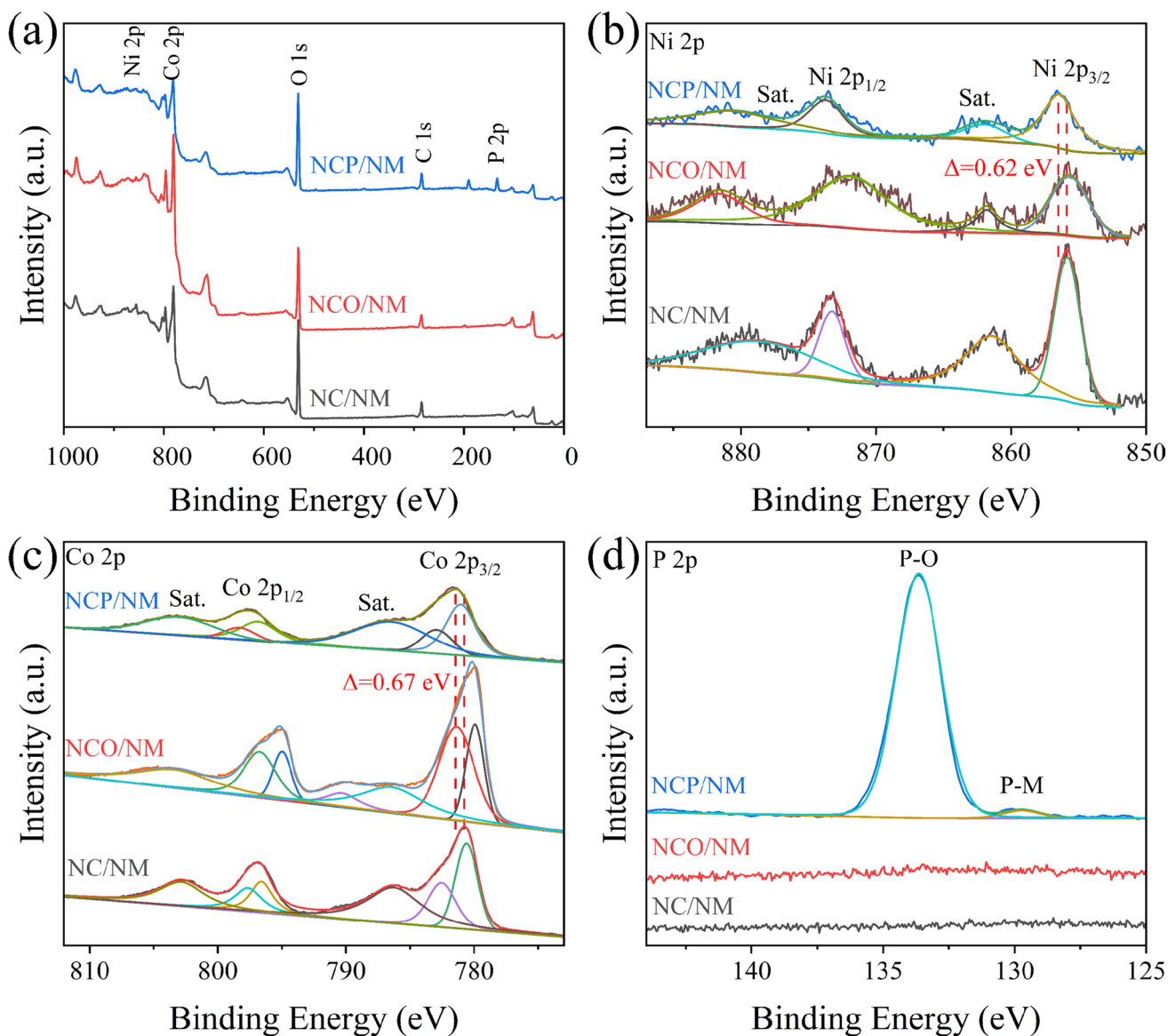
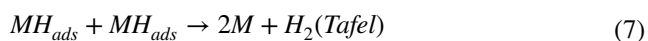


Fig. 5 a XPS survey spectra of NC/NM, NCO/NM, and NCP/NM; High resolution XPS spectra of b Ni 2p, c Co 2p and d P 2p for fabricated electrodes



Correspondingly, the theoretical Tafel slopes in the above steps are 120, 40, and 30 mV dec⁻¹, which are utilized to investigate the kinetic mechanism and rate control steps of the HER process. Because the values are situated in a region of 87 to 95 mV dec⁻¹, HER reaction processes follow a classical Volmer-Heyrosky mechanism. Furthermore, it can be emphasized that the rate-determining step is the Volmer step.

Admittedly, improving the electrocatalytic performance in HER processes can be accomplished via increasing the active sites and the catalytic capacity at the electrode surface. Owing to the linear relationship between the electrochemical

active surface area (ECSA) and C_{dl} , CV tests with different sweep rates in the non-Faraday interval are implemented to estimate the C_{dl} value by the following equation [42]:

$$\Delta j = 2\nu C_{dl} \tag{8}$$

where Δj denotes the corresponding current density difference at the intermediate potential. The CV plots of different samples at different sweep speeds are shown in Fig. S4a–e. On this basis, the calculated results of Δj against ν are plotted in Fig. 6d. The calculated C_{dl} value of NCP/NM (15.28 mF cm⁻²) is higher than other electrodes, reflecting the fact that the sheet electrocatalytic substances which were presented on the electrode surface provided more sites for

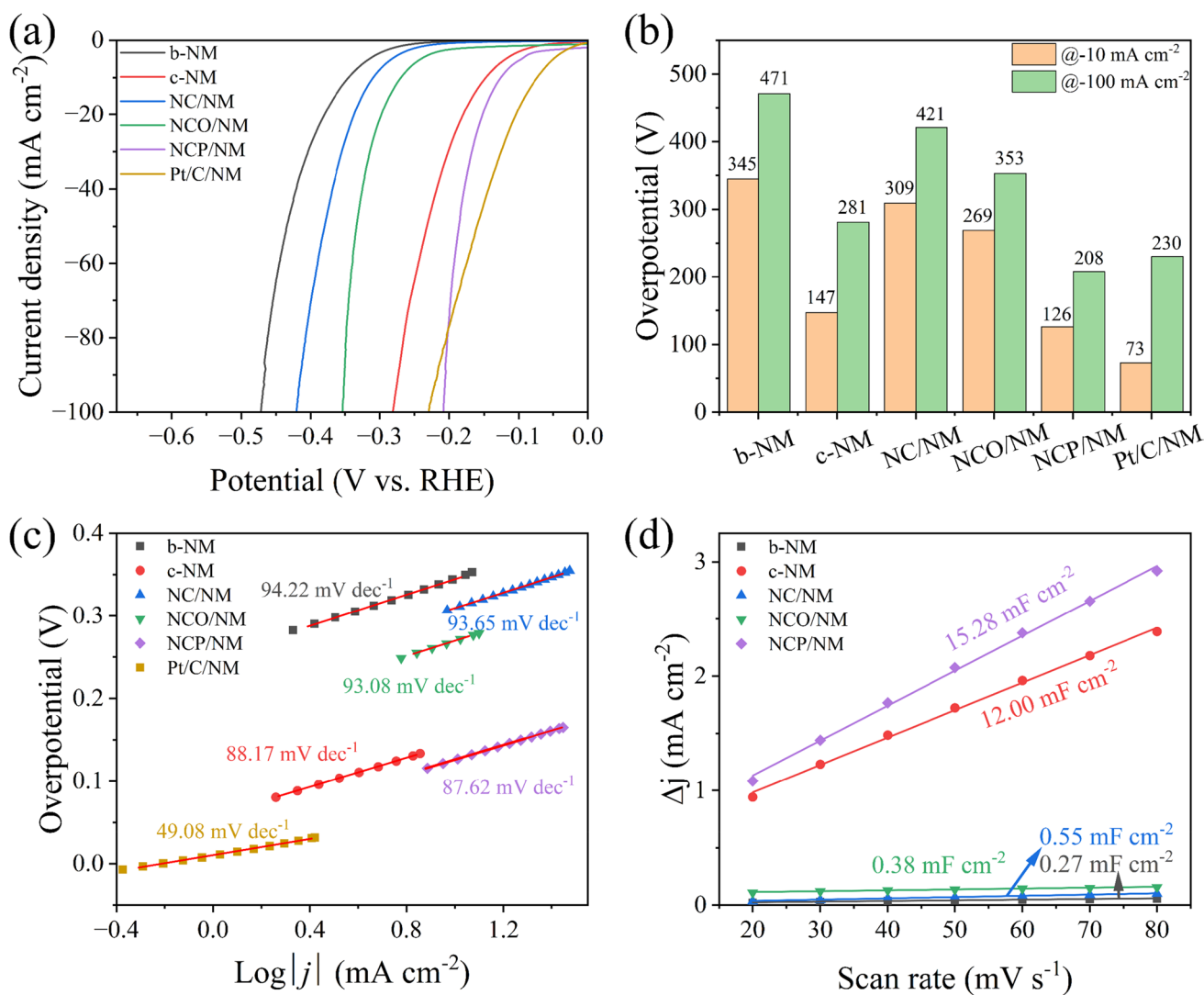


Fig. 6 HER performance of different electrodes in 1 M KOH: **a** IR corrected LSV curves; **b** Required overpotential at cathode current densities of 10 and 100 mA cm⁻²; **c** Tafel plots; **d** Curves of capacitance current versus scan rate

reaction with the electrolyte [43]. Unexpectedly, the C_{dl} value of NCO/NM (0.38 mF cm⁻²) lays between b-NM (0.27 mF cm⁻²) and NC/NM (0.55 mF cm⁻²). Corresponding to their SEM images, the situation can be related to the structural collapse of the electrocatalyst after calcination for a certain period, and the particle size of active material on the surface becomes smaller, resulting in the reduction of ECSA. In Fig. S4f, although the value of NC/NM is over half higher than that of NCO/NM, the current density differences are all lower than NCO/NM. Under the same circumstances, the current response of NCO/NM is more active than that of NC/NM, revealing the difference in their electrocatalytic ability. Besides that, when the current density was normalized to ECSA, as shown in Fig. S5, NCP/NM also exhibits a satisfactory intrinsic activity compared with NC/NM and

NCO/NM, suggesting the good electrical conductivity and fast charge transfer kinetics of the intrinsic active species.

As we know, electrochemical impedance spectroscopy (EIS) is used to analyze the charge transfer kinetics during HER. Figure 7a depicts the Nyquist plots of relative electrodes at 200 mV (vs. RHE) overpotential. The insets show the corresponding equivalent electric circuit (EEC) and the partial enlargement Nyquist plots. A parallel unit consists of a constant phase element (CPE) and a charge transfer resistor (R_{ct}), which is connected in series after the solution resistor (R_s). Although the R_s values of all the electrodes are in a low range of 1–2 Ω due to their favorable electrical contact, there are significant differences in their R_{ct} values. For example, among these electrodes, the R_{ct} value for NCP/NM (1.3 Ω) is the lowest compared with that of NCO/NM

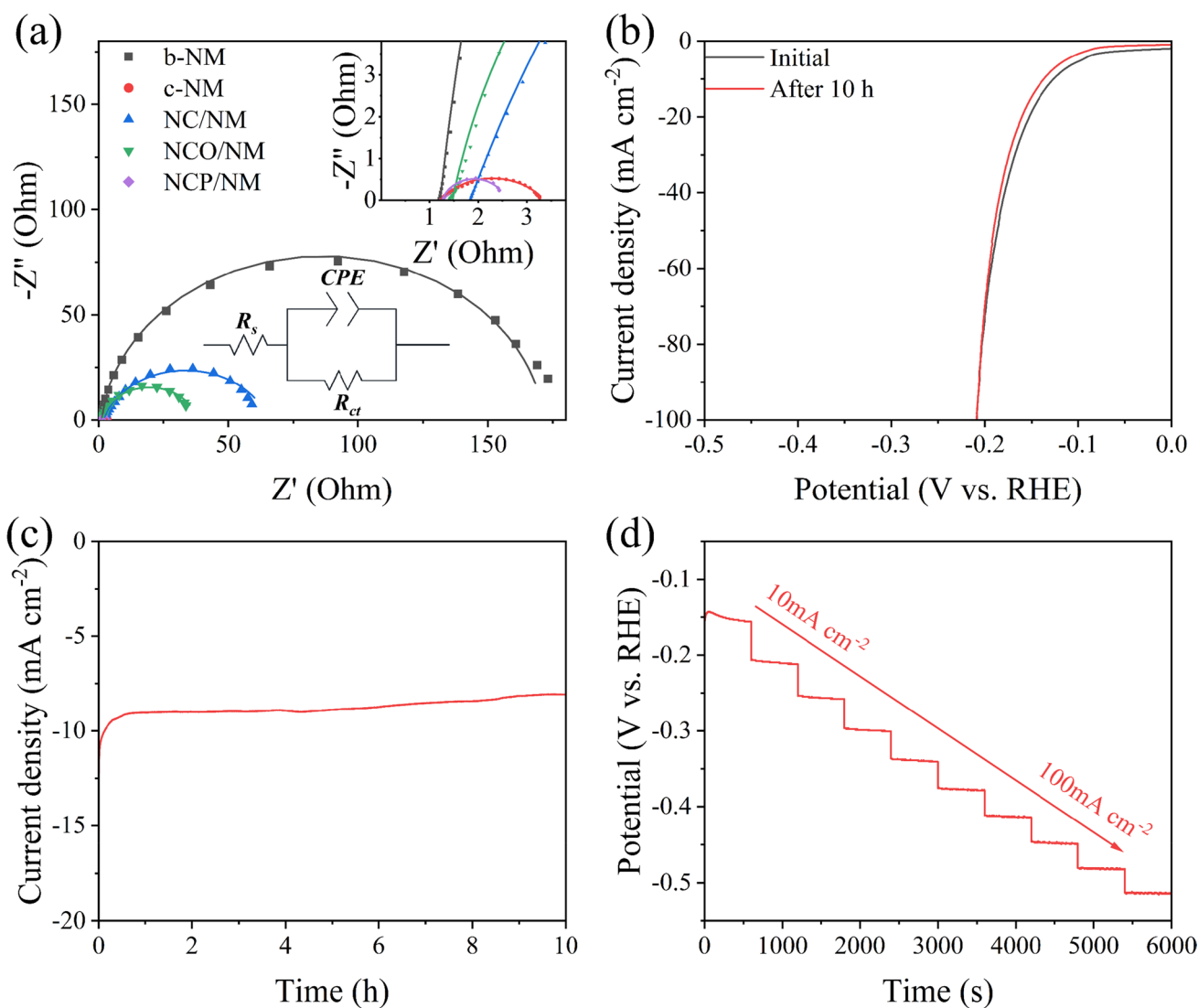


Fig. 7 **a** Nyquist plots of all samples at an overpotential of 200 mV, the bottom inset presents the equivalent electric circuit. **b** Polarization curves for NCP/NM before and after 10 h electrolysis. **c** Chrono-

amperometry curve of NCP/NM conducted at an overpotential of 130 mV. **d** Multi-step chronopotentiometry curve of NCP/NM from 10 mA cm⁻² to 100 mA cm⁻²

(36.4 Ω), NC/NM (63.5 Ω), b-NM (170.4 Ω), and c-NM (2.1 Ω). It is illustrated that the charge transfer kinetics at NCP/NM is significantly improved by the combination of hydrothermal and phosphorylation reactions, suggesting a faster Faraday behavior. NCP/NM is comparable with the commercial c-NM electrode. Furthermore, this is in accordance with the measured LSV of the electrodes. NCP/NM absolutely shows a positive electrocatalytic effect on HER. Therefore, the present NCP/NM was used in the following experiments.

The stability of NCP/NM was investigated for HER by the chronoamperometry method at an overpotential of 130 mV with 10 h in 1 M KOH. It is readily seen that the LSV curves at NCP/NM hardly change even after continuous electrolysis of 10 h, as provided in Fig. 7b, suggesting

a promising stability. The result could also be proved in Fig. 7c, relatively stable current density could be seen at NCP/NM during 10 h, although a slight degradation of the current density was observable towards the end of the test, which could be mainly attributed to the slight shedding of electrocatalyst when hydrogen escapes at the cathode. The stability of NCP/NM was also investigated for HER by the multi-step chronopotentiometry method at a density range from 10 to 100 mA cm⁻² in 1 M KOH. As shown in Fig. 7d, the potential curve at NCP/NM remains good stability in every interval with different current densities, which indicates that the electrode has good electrocatalytic stability in the HER process at different current densities.

After a continuous electrolysis reaction of 10 h, the electrode was characterized by XRD, SEM, TEM, and XPS

techniques to further investigate its structural and morphological stability. The XRD curves display no significant variation in the physical phase after a long stability test as shown in Fig. S6a. The SEM image shows the same nanosheet structure as that of the original NCP/NM in Fig. S6b. Apparently, nanosheet electrocatalysts can be observed in the TEM image (Fig. S6c), which has no significant change compared with the initial sample. Besides, the survey spectrum in Fig. S7a confirms the perseverance of Ni, Co, and P signals after the long-term HER test. High-resolution XPS spectra result in Fig. S7c–d show that the dominant peak positions of Ni 2p, Co 2p, and P 2p for tested NCP/NM are nearly the same as those of the sample before the long-term stability test although the peak intensity changed to a certain extent, proving no change in the species distribution. Therefore, all these demonstrate the desirable stability of the synthesized electrode in terms of crystal structure and micromorphology.

Conclusions

In summary, macroporous NM was used as the substrate, and the NCP/NM electrode was successfully synthesized through a simple two-step process by hydrothermal reaction with ammonia as the solvent and followed by phosphorylation. According to electrochemical characterizations, NCP/NM electrode provided competitive HER performance in 1 M KOH, requiring an overpotential of only 126 mV to produce a current density of 10 mA cm⁻². The electrode also exhibited good suitability and stability in long-term electrolysis. These pleasant electrocatalytic properties can be assigned to fast electron transfer between the electrocatalyst and NM, the synergistic effect of Ni and Co, the positive effect of P-element doping, and the high ECSA. Owing to the advantages of large pore size, rigid material, simple preparation method, and high electrocatalytic activity and durability of NCP/NM, the prepared electrode provides an attractive cathode for hydrogen production in alkaline medium and has potential applications for HER in large-scale industry.

Supplementary information The online version contains supplementary material available at <https://doi.org/10.1007/s11581-023-04915-1>.

Funding This work was supported by the Ministry of Science and Technology of China (Science and Technology to Boost Economy 2020 Key Project, SQ2020YFF0412719 and SQ2020YFF0404901), the Key Research and Development and Transformation Program Funding in Qinghai Province (2021-GX-105), and Anhui Province Key Research and Development Plan (202104e11020005).

Data Availability Data available on request from the authors.

References

- Sazali N (2020) Emerging technologies by hydrogen: a review. *Int J Hydrogen Energy* 45:18753–18771. <https://doi.org/10.1016/j.ijhydene.2020.05.021>
- Li B, Haneklaus N (2021) The role of renewable energy, fossil fuel consumption, urbanization and economic growth on CO₂ emissions in China. *Energy Rep* 7:783–791. <https://doi.org/10.1016/j.egy.2021.09.194>
- Møller KT, Jensen TR, Akiba E, Li H, Wen (2017) Hydrogen – a sustainable energy carrier. *Prog Nat Sci Mater Int* 27:34–40. <https://doi.org/10.1016/j.pnsc.2016.12.014>
- Brandon NP, Kurban Z (2017) Clean energy and the hydrogen economy. *Phil Trans R Soc A Math Phys Eng Sci* 375:20160400. <https://doi.org/10.1098/rsta.2016.0400>
- Du X, Shao Q, Zhang X (2019) Cu–Co–M arrays on Ni foam as monolithic structured catalysts for water splitting: effects of co-doped S-P. *Dalt Trans* 48:1322–1331. <https://doi.org/10.1039/C8DT04731F>
- Tarhan C, Çil MA (2021) A study on hydrogen, the clean energy of the future: hydrogen storage methods. *J Energy Storage* 40:102676. <https://doi.org/10.1016/j.est.2021.102676>
- Yin Z, Xu H, Chen Y et al (2022) Experimental simulate on hydrogen production of different coals in underground coal gasification. *Int J Hydrogen Energy* 48:6975–6985. <https://doi.org/10.1016/j.ijhydene.2022.03.205>
- Yan Q, Liu Z, Bai X et al (2022) In situ formed edge-rich Ni₃S₂-NiOOH heterojunctions for oxygen evolution reaction. *J Electrochem Soc* 169:054532. <https://doi.org/10.1149/1945-7111/ac7083>
- Zhang JJ, Li MY, Li X et al (2022) Chromium-modified ultrathin CoFe LDH as high-efficiency electrode for hydrogen evolution reaction. *Nanomaterials* 12:1–12. <https://doi.org/10.3390/nano12071227>
- Wu D, Kusada K, Yamamoto T et al (2020) On the electronic structure and hydrogen evolution reaction activity of platinum group metal-based high-entropy-alloy nanoparticles. *Chem Sci* 11:12731–12736. <https://doi.org/10.1039/d0sc02351e>
- Huang J, Wang S, Nie J et al (2021) Active site and intermediate modulation of 3D CoSe₂ nanosheet array on Ni foam by Mo doping for high-efficiency overall water splitting in alkaline media. *Chem Eng J* 417:128055. <https://doi.org/10.1016/j.cej.2020.128055>
- Jiang L, Ji SJ, Xue HG, Suen NT (2020) HER activity of M_xNi_{1-x} (M = Cr, Mo and W; x ≈ 0.2) alloy in acid and alkaline media. *Int J Hydrogen Energy* 45:17533–17539. <https://doi.org/10.1016/j.ijhydene.2020.04.242>
- Gomez MJ, Franceschini EA, Lacconi GI (2018) Ni and Ni_xCo_y alloys electrodeposited on stainless steel AISI 316L for hydrogen evolution reaction. *Electrocatalysis* 9:459–470. <https://doi.org/10.1007/s12678-018-0463-5>
- Kim J, Jung H, Jung SM et al (2021) Tailoring binding abilities by incorporating oxophilic transition metals on 3D nanostructured Ni arrays for accelerated alkaline hydrogen evolution reaction. *J Am Chem Soc* 143:1399–1408. <https://doi.org/10.1021/jacs.0c10661>
- Wu Y, Chen X, Su L et al (2022) Three-dimensional self-supporting Ni₂P-Ni₁₂P₅/NF heterostructure as an efficient electrocatalyst to enhance hydrogen evolution reaction. *Ionics* 28:3935–3944. <https://doi.org/10.1007/s11581-022-04631-2>
- Liu G, Bai H, Ji Y et al (2019) A highly efficient alkaline HER Co–Mo bimetallic carbide catalyst with an optimized Mo d-orbital electronic state. *J Mater Chem A* 7:12434–12439. <https://doi.org/10.1039/C9TA02886B>
- Lee Y, Ahn JH, Shin S et al (2022) Metal-nitrogen intimacy of the nitrogen-doped ruthenium oxide for facilitating electrochemical hydrogen production. *Appl Catal B Environ* 303:120873. <https://doi.org/10.1016/j.apcatb.2021.120873>
- Charnetskaya E, Chatti M, Kerr BV et al (2022) Intrinsic catalytic activity for the alkaline hydrogen evolution of layer-expanded MoS₂ functionalized with nanoscale Ni and Co sulfides. *ACS*

- Sustain Chem Eng 10:7117–7133. <https://doi.org/10.1021/acssuschemeng.2c01243>
19. Smialkowski M, Tetzlaff D, Hensgen L et al (2021) Fe/Co and Ni/Co-pentlandite type electrocatalysts for the hydrogen evolution reaction. *Chinese J Catal* 42:1360–1369. [https://doi.org/10.1016/S1872-2067\(20\)63682-8](https://doi.org/10.1016/S1872-2067(20)63682-8)
 20. Cao X, Wang T, Jiao L (2021) Transition-metal (Fe, Co, and Ni)-based nanofiber electrocatalysts for water splitting. *Adv Fiber Mater* 3:210–228. <https://doi.org/10.1007/s42765-021-00065-z>
 21. Zhang D, Zhao H, Huang B et al (2019) Advanced ultrathin RuPdM (M = Ni, Co, Fe) nanosheets electrocatalyst boosts hydrogen evolution. *ACS Cent Sci* 5:1991–1997. <https://doi.org/10.1021/acscentsci.9b01110>
 22. Zhou J, Dou Y, He T et al (2021) Revealing the effect of anion-tuning in bimetallic chalcogenides on electrocatalytic overall water splitting. *Nano Res* 14:4548–4555. <https://doi.org/10.1007/s12274-021-3370-7>
 23. Peng S, Gong F, Li L et al (2018) Necklace-like multishelled hollow spinel oxides with oxygen vacancies for efficient water electrolysis. *J Am Chem Soc* 140:13644–13653. <https://doi.org/10.1021/jacs.8b05134>
 24. Wang Z, Liu H, Ge R et al (2018) Phosphorus-doped Co₃O₄ nanowire array: a highly efficient bifunctional electrocatalyst for overall water splitting. *ACS Catal* 8:2236–2241. <https://doi.org/10.1021/acscatal.7b03594>
 25. Cheng L, Zhang R, Lv W, et al (2020) Surface phosphation of 3D NiCo₂O₄ nanowires grown on Ni foam as an efficient bifunctional catalyst for water splitting. *Nano* 15:2050024. <https://doi.org/10.1142/S1793292020500241>
 26. Sahasrabudhe A, Dixit H, Majee R, Bhattacharyya S (2018) Value added transformation of ubiquitous substrates into highly efficient and flexible electrodes for water splitting. *Nat Commun* 9:2014. <https://doi.org/10.1038/s41467-018-04358-7>
 27. Niu S, Li S, Du Y et al (2020) How to reliably report the overpotential of an electrocatalyst. *ACS Energy Lett* 5:1083–1087. <https://doi.org/10.1021/acscenergylett.0c00321>
 28. Li M, Tao L, Xiao X et al (2019) Hybridizing NiCo₂O₄ and amorphous Ni_xCo_y layered double hydroxides with remarkably improved activity toward efficient overall water splitting. *ACS Sustain Chem Eng* 7:4784–4791. <https://doi.org/10.1021/acssuschemeng.8b05044>
 29. Shang X, Chi JQ, Lu SS et al (2017) Hierarchically three-level Ni₃(VO₄)₂@NiCo₂O₄ nanostructure based on nickel foam towards highly efficient alkaline hydrogen evolution. *Electrochim Acta* 256:100–109. <https://doi.org/10.1016/j.electacta.2017.10.017>
 30. Gong Y, Yang Z, Lin Y et al (2018) Hierarchical heterostructure NiCo₂O₄@CoMoO₄/NF as an efficient bifunctional electrocatalyst for overall water splitting. *J Mater Chem A* 6:16950–16958. <https://doi.org/10.1039/c8ta04325f>
 31. Su P, Liu H, Jin Z (2022) Metal organic framework-derived Co₃O₄/NiCo₂O₄ hollow double-shell polyhedrons for effective photocatalytic hydrogen generation. *Appl Surf Sci* 571:151288. <https://doi.org/10.1016/j.apsusc.2021.151288>
 32. Yang JH, Xu X, Chen M et al (2021) Morphology-controllable nanocrystal β-Ni(OH)₂/NF designed by hydrothermal etching method as high-efficiency electrocatalyst for overall water splitting. *J Electroanal Chem* 882:115035. <https://doi.org/10.1016/j.jelechem.2021.115035>
 33. Wang J, Xuan H, Meng L et al (2022) Facile synthesis of N, S co-doped CoMoO₄ nanosheets as high-efficiency electrocatalysts for hydrogen evolution reaction. *Ionics* 28:4685–4695. <https://doi.org/10.1007/s11581-022-04707-z>
 34. Sekar P, Muruges N, Shanmugam R et al (2021) Phosphazene-based covalent organic polymer decorated with NiCo₂O₄ nanocuboids as a trifunctional electrocatalyst: a unique replacement for the conventional electrocatalysts. *ACS Appl Energy Mater* 4:9341–9352. <https://doi.org/10.1021/acsaem.1c01550>
 35. Zhang H, Zhang J, Li Y et al (2019) Continuous oxygen vacancy engineering of the Co₃O₄ layer for an enhanced alkaline electrocatalytic hydrogen evolution reaction. *J Mater Chem A* 7:13506–13510. <https://doi.org/10.1039/c9ta03652k>
 36. Cao J, Jiao Z, Zhu R et al (2022) Enhancing hydrogen evolution through urea electrolysis over Co-doped Ni-P-O film on nickel foam. *J Alloys Compd* 914:165362. <https://doi.org/10.1016/j.jallcom.2022.165362>
 37. Wang L, Zhao Y, Huang Z, et al (2022) Interfacial regulation of electron-enhanced Co₂P–CuP₂ sheet-like heterostructure as a robust bifunctional electrocatalyst for overall water splitting and Zn–H₂O cell. *ChemCatChem* 14:e202101933. <https://doi.org/10.1002/cctc.202101933>
 38. Tian R, Wang F, Zou C et al (2023) Modulating organic ligands to construct 2D–3D-hybrid porous P-doped metal-organic frameworks electrocatalyst for overall water splitting. *J Alloys Compd* 933:167670. <https://doi.org/10.1016/j.jallcom.2022.167670>
 39. Barati Darband G, Lotfi N, Aliabadi A, et al (2021) Hydrazine-assisted electrochemical hydrogen production by efficient and self-supported electrodeposited Ni-Cu-P@Ni-Cu nano-micro dendrite catalyst. *Electrochim Acta* 382:138335. <https://doi.org/10.1016/j.electacta.2021.138335>
 40. Anantharaj S, Noda S (2022) How properly are we interpreting the Tafel lines in energy conversion electrocatalysis? *Materials Today Energy* 29:101123. <https://doi.org/10.1016/j.mtener.2022.101123>
 41. Fan X, Liu C, Wu M et al (2022) Synergistic effect of dual active sites over Ru/A-Moc for accelerating alkaline hydrogen evolution reaction. *SSRN Electron J* 318:101123. <https://doi.org/10.2139/ssrn.4129299>
 42. Liu H, Zeng S, He P et al (2019) Samarium oxide modified Ni-Co nanosheets based three-dimensional honeycomb film on nickel foam: a highly efficient electrocatalyst for hydrogen evolution reaction. *Electrochim Acta* 299:405–414. <https://doi.org/10.1016/j.electacta.2018.12.169>
 43. Ye F, Yang Y, Liu P, et al (2022) In-situ porous flake heterostructured NiCoP/Ni foam as electrocatalyst for hydrogen evolution reaction. *Electrochim Acta* 423:140578. <https://doi.org/10.1016/j.electacta.2022.140578>

Publisher's note Springer Nature remains neutral with regard to jurisdictional claims in published maps and institutional affiliations.

Springer Nature or its licensor (e.g. a society or other partner) holds exclusive rights to this article under a publishing agreement with the author(s) or other rightsholder(s); author self-archiving of the accepted manuscript version of this article is solely governed by the terms of such publishing agreement and applicable law.